Chapter 5

GNSS Application in Retrieving Sea Wind Speed

Dongkai Yang and Feng Wang

Additional information is available at the end of the chapter

http://dx.doi.org/10.5772/intechopen.74149

Abstract

In traditional Global Navigation Satellite System (GNSS) application, the reflected GNSS signals from Earth's surface generally are considered as an interference source to be suppressed or removed. Recently, a new idea which treats the reflected GNSS signal as opportunity source of remote sensing has been proposed to monitor Earth's physical parameters. This technique is called as GNSS-Reflectometry (GNSS-R) which has the advantages of low-power, -mass and -cost. With the development and modernization of GPS, Galileo, GLONASS, and BeiDou system, spaceborne GNSS could significantly improve the temporal-spatial resolution by receiving and processing the reflected signal from multiple satellites. This chapter mainly describes this new bi-static remote sensing technique. First, basic theories of GNSS-R including spatial geometry, polarization, and scattering model of reflected signal are discussed; second, spaceborne receivers and fast-response processing methods are reviewed and analyzed; finally, the empirical models retrieving wind speed are proposed and demonstrated using the DDM data from the UK-TechDomeSat-1 satellite. Based on the discussion of this chapter, it could be concluded that although GNSS-R still has some key challenges which have to be addressed, it could be an optimal choice of remote sensing in some special conditions, such as the tropical cyclone.

Keywords: GNSS-Reflectometry, remote sensing, delay-Doppler maps, wind speed

1. Introduction

Sea wind speed is an important parameter which impacts the ocean circulation and global climate. Moreover, tropical cyclones, as one of the most serious natural disasters, interrupt infrastructure and endanger life safety [1]. For these reasons, it is important to monitor sea wind speed to study and forecast some complex weather. Traditional tools, such as buoys,

could provide long-term observation, however, have low spatial sampling. The spaceborne microwave remote sensing devices such as radar altimeter [2], scatterometer [3], and radiometer [4], provide all weather and all day observation of global wind speed. However, high-mass, -power, and -cost equipment limit their application in commercial remote sensing based on the single-function microsatellite. GNSS not only provides the positioning, velocity, and timing (PVT), but also could be considered as the opportunity sources of remote sensing to observe Earth physical parameters. This observation is known as GNSS-Reflectometry which uses GNSS signal reflected off Earth's surface to observe Earth's physical parameters. It has been demonstrated that GNSS-R could have been utilized to measure sea wind speed [5], sea surface height [6], sea ice [7], and soil moisture [8] from ground-based, airborne, and spaceborne platforms in past 20 years. Compared to traditional remote sensing ways, GNSS-R has the advantages of the low-cost and low-power, because only a receiver is needed. Spaceborne GNSS-R could improve the global temporal-spatial resolution because there are more than 100 GNSS satellites in orbit or planned. In addition, the temporal-spatial resolution could be further improved by microsatellite network.

The idea of using reflected GNSS signal from Earth's surface for remote sensing was discussed by Hall and Cordey in 1988 [9]. In 1993, Martin-Neria proposed the concept of PAssive Reflectometry and Interferometry System (PARIS) to use GNSS signal reflected off the ocean for the measurement of ocean altimetry [10]. In 1994, Auber et al. detected GNSS signal reflected off the ocean from an aircraft platform [11]. In 1998, Garrison and Katzberg demonstrated that reflected global positioning system (GPS) signal could measure sea wind speed through an aircraft experiment [12]. The first collection of reflected GPS signal from spaceborne platform was reported in 2002 [13]. The use of reflected GPS signal acquired by UK-DMC satellite is recognized as the first spaceborne experiment to measure wind speed [14]. After the success of the UK-DMC, UK TechDemoSat-1 [15], PARIS-IoD [16], GEROS-ISS [17], and CYGNSS [18] were planned and developed to further demonstrate the feasibility of using reflected GNSS signal to observe Earth parameters. Especially, CYGNSS mission aims to improve intensity forecasting by sensing sea wind speed in the inner core of tropical cyclones using a constellation of eight microsatellites.

The basic product of GNSS-R is the so-called Delay Waveform or delay-Doppler map (DDM) of reflected GNSS signal, which describes the distribution of power level in delay or delay-Doppler domain. Based on the bi-static radar equation and the geometric optics limit of the Kirchhoff approximation, Zavorotny and Voronovich developed the theoretical power model of the scattered GNSS signal as a function of the geometrical and environmental parameters [19]. To simulate DDM, the Z-V model can be implemented by defining the scenario in a reference system and evaluating the functions inside the integrand to compute the integral for every delay and Doppler bin. However, such approach is extremely time- and resource-consuming, especially for spaceborne scenario. In [20], a new and efficient method to compute DDM was proposed based on the derivation of explicit expressions of the space coordinates as a function of the delay offset and Doppler shift. The realistic problem that the noisy DDM measurements should be generated motivated the model and the simulator to produce DDM time series based on a multiple-input-multiple-output filter bank [21]. Other approaches of simulating DDM generate a synthetic sea surface with accurate temporal-spatial correlations and model the time evolution of the scattered signal. In [22], Clarizia et al. presented a new

facet-based approach to model the scattering of GNSS signal from the synthetic sea surface and used it to compute DDM for the spaceborne scenario. In practice, the DDM is generated by correlating the reflected GNSS signal with the locally generated replicas at different delay offset and Doppler shift. In [23], a delay/Doppler-mapping hardware/software receiver was presented. A real-time instrument called as GPS open-loop differential real-time receiver (GOLD-RTR) was designed and developed to gather the complex correlations of reflected GPS signal in [24]. To conform the development of spaceborne GNSS-R mission, spaceborne GNSS-R receivers have been designed and developed, such as Space GNSS Receiver Remote Sensing Instrument (SGR-ReSI) [25] and GNSS-REflectometry, Radio Occultation, and Scatterometry (GEROS) [26] for UK-TDS-1 satellite and International Space Station.

The purpose of remote sensing is to determine the Earth's physical parameters, for which it is the key technology to develop the link between GNSS-R observable and the Earth's physical parameters. Some algorithms have been proposed to retrieve sea wind speed using GNSS-R. The first type of method is to fit the measured Delay Waveform or DDM to theoretical one. In [27], the trailing edge slope and the complete shape of the Delay Waveform were used to fit the analytical models to estimate wind speed. A 2-D least-squares fitting approach was given to retrieve wind field by fitting the simulated DDM to space-based measured one from UK-DMC satellite [28]. These methods based on fitting are time-and resource-consuming. The second type of method is to directly link wind speed and different Delay Waveform or DDM observable by the regression. In 2013, Rodrigues-Alvarez et al. reported their airborne experiment results in which four DDM observable including weighted area, 2-norm Euclidean distance, distance from the geometric center to the maximum value of DDM, and 1-norm Euclidean distance were defined and linked with the wind speed [29]. First results of the retrieved wind speed using the data from UK TechDemoSat-1 satellite were presented in [30], where in-situ wind from Advanced Scatterometer (ASCAT) and the bi-static scattering coefficient derived from peak DDM using bi-static radar equation are utilized to develop a wind speed retrieval algorithm and the accuracy of 2.2 m/s could be obtained in range from 3 to 18 m/s. To improve retrieval accuracy of high wind speed and spatial resolution for CYGNSS mission, Rodriguez-Alvarez defined the generalized linear DDM observable based on maximum signal-to-noise ratio (SNR), minimum variance of wind speed, and principal component analysis (PCA) to develop relationships with wind speed and found that the observable based on PCA had the best performance [31]. The retrieval algorithm proposed by M. P. Clarizia in 2014 was used to produce the Level 2 wind speed data product of CYGNSS mission in [32], in which several additional processing steps were added to correct the influence of incident angle and adaptively select the parameters of the algorithm to improve the retrieving accuracy [32]. The algorithms for CYGNSS mission have limited the spatial resolution in the region of 25 km $\times$ 25 km. These retrieval algorithms above all provide a single wind speed descriptor in the overall observation region. The third type of method is based on the mapping between the physical space and the delay-Doppler domain. In [33], an algorithm to retrieve the bi-static scattering coefficient distribution over the observation region from measured DDM using the deconvolution was proposed. D. Schiavulli demonstrated the validity and feasibility of this approach using UK-TechDemoSat-1 data [34].

This chapter will illustrate the GNSS application in retrieving wind speed using spaceborne GNSS-R. Section 2 will discuss the basic theories of GNSS-R including the observation

geometry, the polarization, and the model of reflected GNSS signal. Section 3 will present some typical spaceborne GNSS-R receivers and processing methods of reflected GNSS signal. The explicit retrieval algorithms based on the regression will be developed in Section 4. Finally, the conclusion of this chapter will be addressed in Section 5.

2. Basic theory of GNSS-R

2.1. Geometry

GNSS-R works as a bi-static radar in which the transmitter and the receiver are separated in the spatial distribution. It is noted that when GNSS-R receivers allow to track the scattered signal from different GNSS satellites, the system is called as multi-static radar as shown in **Figure 1**, in which for each GNSS satellite, bi-static observation occurs at different azimuth angle, and creates a glistening zone. To simplify observation geometry of GNSS-R, a bi-static geometry could be developed as **Figure 2**, in which (1) the coordinate origin is at Earth's core; (2) the YOZ plane is in the incident plane of GNSS signal; (3) Z axis has the same direction with the normal of the tangent plane of the specular point; and (4) it is assumed that Earth, the orbits of GNSS and Low Earth Orbit (LEO) satellite are circular. In **Figure 2**, h_r and h_t are the heights of LEO and GNSS satellite; R_e is the Earth radius; θ is the incident angle of GNSS signal. In the coordinate system, the positioning of GNSS and LEO satellite are given as

$$\mathbf{T} = (0 \;\; D\sin\theta \;\; R_e + D\cos\theta) \tag{1}$$

$$\mathbf{R} = (\,0 \quad -d\sin\theta \quad R_e + D\cos\theta\,) \tag{2}$$

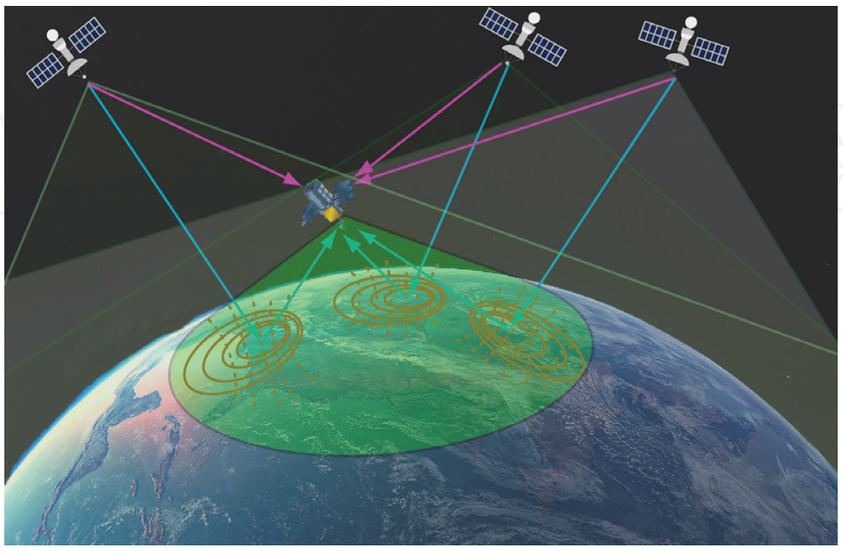

Figure 1. Illustration of multi-static GNSS-R.

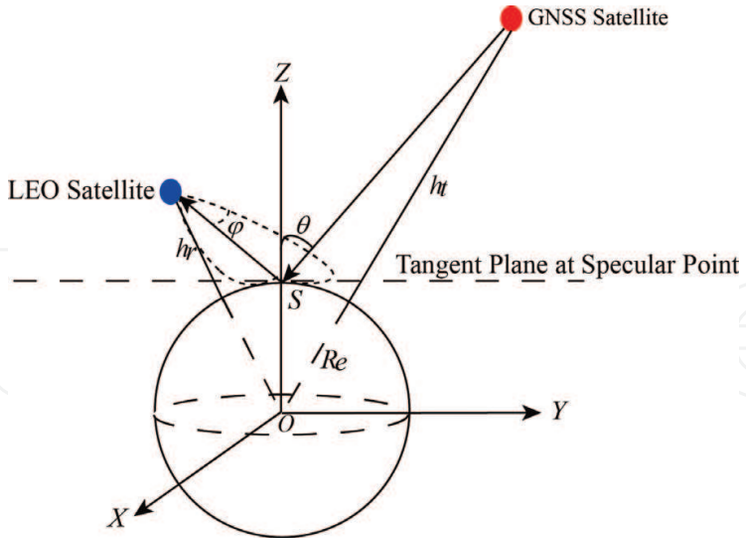

Figure 2. Scattering scenario and local coordinate system of GNSS-R.

where D and d are the distance from GNSS and LEO satellite to the specular point, and are expressed as

$$D = -R_e\cos\theta + \sqrt{(h_t + R_e)^2 - R_e^2\sin^2\theta} \tag{3}$$

$$d = -R_e\cos\theta + \sqrt{(h_r + R_e)^2 - R_e^2\sin^2\theta} \tag{4}$$

The coordinate of scattering unit $\boldsymbol{\rho}$ could be represented as

$$\boldsymbol{\rho} = \begin{pmatrix} \delta_x & \delta_y & 1 \end{pmatrix} \cdot R_e \tag{5}$$

where δ_x and δ_y are the included angles between the projection of the connection line of $S_{x,y}$ and the coordinate origin at the XOZ and YOZ plane. From the above discussion, when the height of GNSS and LEO satellite, and the incident angle of GNSS signal are known, the geometry of GNSS-R could be determined.

2.2. Polarization of reflected GNSS signal

When Right-Hand Circular Polarization (RHCP) GNSS signal occurs reflection phenomenon, the polarization is changed. The Fresnel coefficients of RHCP and LHCP (Left-Hand Circular Polarization) are expressed as the combination of the vertical and horizontal polarization as

$$\Re_{RR} = \Re_{RR} = \frac{1}{2}(\Re_{VV} + \Re_{HH}) \tag{6}$$

$$\Re_{RL} = \Re_{LR} = \frac{1}{2}(\Re_{VV} - \Re_{HH}) \tag{7}$$

The Fresnel coefficients of vertical and horizontal polarization are computed as

$$\Re_{VV} = \frac{\varepsilon\cos\theta - \sqrt{\varepsilon - \sin^2\theta}}{\varepsilon\cos\theta + \sqrt{\varepsilon - \sin^2\theta}} \tag{8}$$

$$\Re_{HH} = \frac{\cos\theta - \sqrt{\varepsilon - \sin^2\theta}}{\cos\theta + \sqrt{\varepsilon - \sin^2\theta}} \tag{9}$$

Figure 3 gives the simulated Fresnel coefficients of RHCP and LHCP for GPS L1 signal, when sea surface temperature is 25° and sea surface salinity is 35 psu. From the figure, it could be seen that as the incident angle increases, the Fresnel coefficients of RHCP and LHCP show decreasing and increasing trends, respectively. This illustrates that at nadir and small incident angle, the LHCP signal dominates GNSS signal reflected off the sea surface. Therefore, the combination of LHCP and RHCP antenna or only LHCP antenna is used to receive reflected GNSS signal from the sea surface.

2.3. Model of reflected GNSS signal

The signal reflected from the sea surface is described as [21]

$$u_r(\mathbf{R},t) = A_R \exp(-2\pi j f_0 t) \iint G(\boldsymbol{\rho}) a\left(t - \frac{D+d}{c}\right) g(\mathbf{R},t) d^2\boldsymbol{\rho} \tag{10}$$

where f_0 is the carrier frequency; A_R is the amplitude of reflected signal; G is the pattern of receiving antenna; $a(t)$ is the baseband spreading signal; c is the speed of light; $g(\mathbf{R},t)$ is the function as

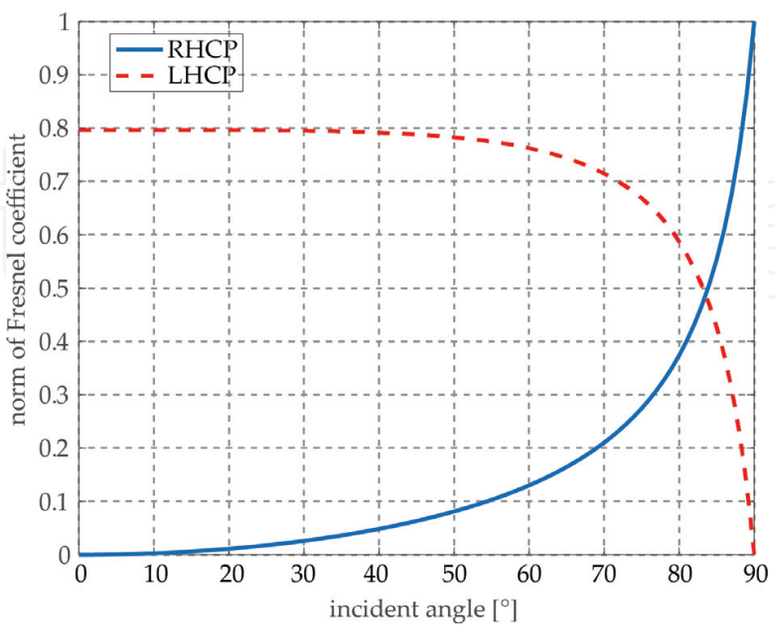

Figure 3. Relationship between the amplitude of RHCP and LHCP Fresnel coefficient and incident angle.

$$g(\mathbf{R},t) = -\frac{\Re}{4\pi j D(\boldsymbol{\rho})d(\boldsymbol{\rho})}\exp[jk(D(\boldsymbol{\rho})+d(\boldsymbol{\rho}))]\frac{\mathbf{q}^2(\boldsymbol{\rho})}{\mathbf{q}_\perp^2(\boldsymbol{\rho})} \tag{11}$$

where $\Re$ is the Fresnel coefficient discussed in Section 2.2; $D(\boldsymbol{\rho})$ and $d(\boldsymbol{\rho})$ are the distance from GNSS and LEO satellite to scattering unit $\boldsymbol{\rho}$; $\mathbf{q}$ is the scattering vector defined as

$$\mathbf{q}=(\,\mathbf{q}_\perp \quad q_z\,)=k\left(\frac{\mathbf{d}(\boldsymbol{\rho})}{d(\boldsymbol{\rho})}+\frac{\mathbf{D}(\boldsymbol{\rho})}{D(\boldsymbol{\rho})}\right) \tag{12}$$

where k is the wavenumber of GNSS signal; $\mathbf{D}(\boldsymbol{\rho})$ and $\mathbf{d}(\boldsymbol{\rho})$ are the vectors from scattering unit $\boldsymbol{\rho}$ to GNSS and LEO satellite. The receiver processes reflected GNSS signal by cross-correlating with local replicas over a range of delay and Doppler as

$$Y(\tau,f,t) = \int_t^{t+T_I} u_r(\mathbf{R},t)p(t-\tau)\exp\left[2\pi j\left(f_0+f\right)t\right]dt \tag{13}$$

where T_I is the coherent integration time. The output of spaceborne GNSS-R receiver is the power level as a function of delay offset and Doppler shift. To reduce the influence of thermal and speckle noise, the successive snapshots are averaged as

$$\left\langle |Y(\tau,f)|^2 \right\rangle = \frac{1}{\mathrm{T_{incoh}}}\int_0^{\mathrm{T_{incoh}}} |Y(\tau,f,t)|^2 dt \tag{14}$$

where $\mathrm{T_{incoh}}$ is the incohernt integration time. Zavorotny and Voronovivh first derived the expression (14) as [19]

$$\left\langle |Y(\tau,f)|^2 \right\rangle = A_R^2 T_I^2 \iint \frac{G^2(\boldsymbol{\rho})\Lambda^2(\tau-\tau(\boldsymbol{\rho}))\cdot \mathrm{sinc}^2(f-f(\boldsymbol{\rho}))}{4\pi D(\boldsymbol{\rho})^2 d(\boldsymbol{\rho})^2}\sigma_0^2 d^2\boldsymbol{\rho} \tag{15}$$

where $\tau(\boldsymbol{\rho})$ and $f(\boldsymbol{\rho})$ are the delay and Doppler frequency of scattering unit $\boldsymbol{\rho}$; σ_0 is the normalized bi-static cross section and it is as follows:

$$\sigma_0 = \pi|\Re|^2\frac{q_z^4}{\mathbf{q}_\perp^4}P_{\mathrm{pdf}}\left(-\frac{\mathbf{q}_\perp}{q_z}\right) \tag{16}$$

where $P_{\mathrm{pdf}}(\cdot)$ is the probability density function of mean square slopes of the sea surface, and could be usually assumed as a 2-D Gaussian distribution. **Figure 4** shows the normalized DDM distribution for the wind speed of 5 m/s and 15 m/s, in which both DDMs show clear horseshoe shapes; moreover, with the increase in wind speed, DDM spreads to larger delay and Doppler. Different scattering units have different delay and Doppler frequency; hence, DDM not only represents the distribution in delay-Doppler domain, but also indicates the distribution in sea surface as illustrated in **Figure 5**. In practice, the one cell in delay-Doppler domain associates to two spatial solutions, i.e., the mapping between the space and the delay-Doppler domain exists with ambiguity. To reduce this mapping ambiguity, the one approach is to tilt the downward antenna beam away from the specular reflection point.

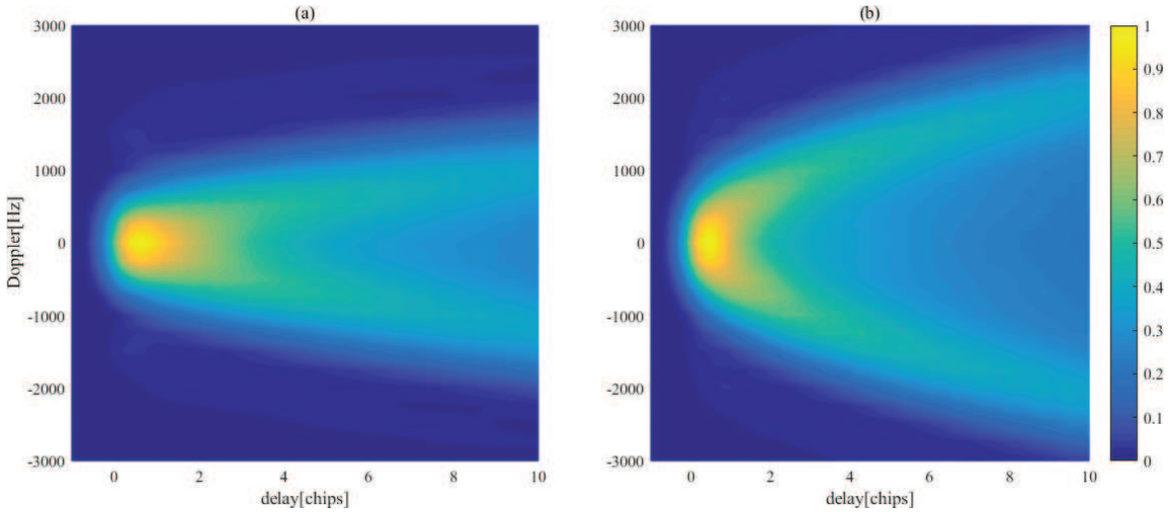

Figure 4. Normalized DDM for the wind speed of (a) 5 m/s and (b) 15 m/s, when the height of LEO satellite is 657 km and the incident angle of GNSS signal is 60°.

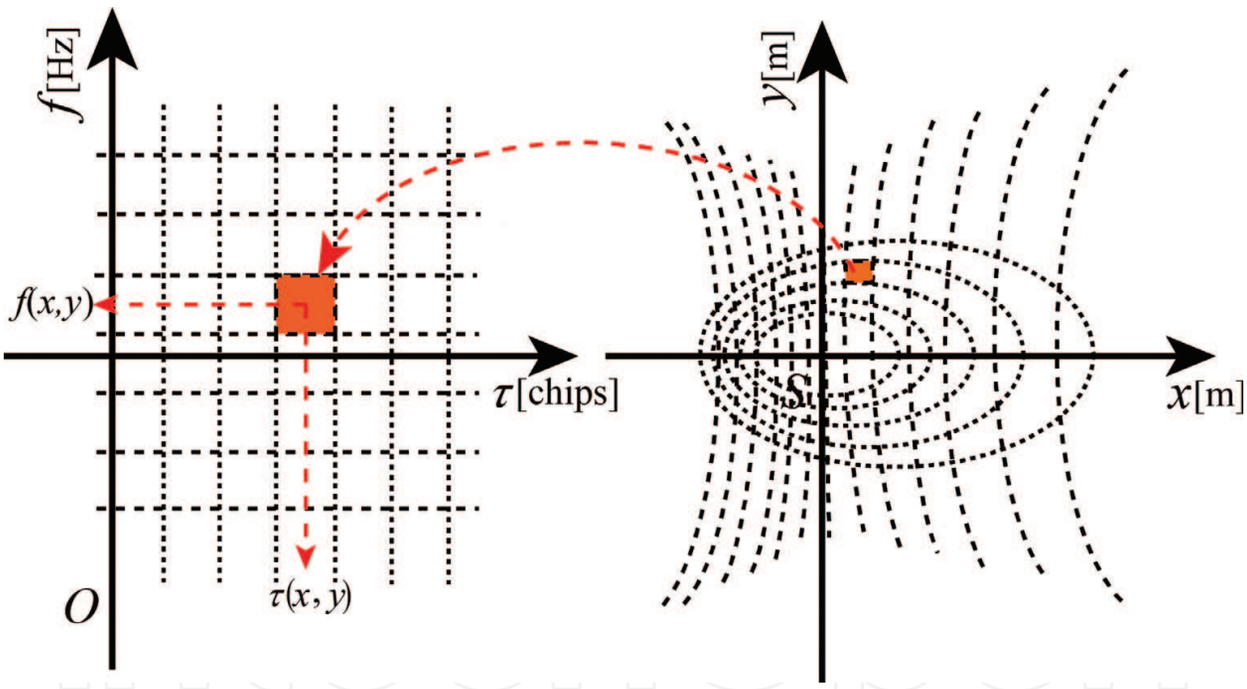

Figure 5. Mapping from space to the delay-Doppler domain.

The other approach is using two separate antennas from two different viewing angles to observe an ocean surface region.

3. Processing of GNSS reflected signal

The GNSS-R receiver is a processing unit to cross-correlate reflected GNSS signal with locally generated replicas. Spaceborne GNSS-R receiver not only requires the capacity of

processing reflected GNSS signal in real-time, but also with low-mass, -power and -cost. At present, some research groups have developed spaceborne GNSS receivers to meet their spaceborne missions.

3.1. Existing receivers

3.1.1. UK-DMC

To promote the development of spaceborne GNSS-R and explore its prospect of commercial application, Surrey Satellite Technology Ltd. (SSTL) designed and developed spaceborne GPS-R receiver which would be carried on UK-DMC. This receiver which was implemented based on spaceborne GPS receiver of SSTL consisted of a zenith antenna to receive direct GPS signal, a LCHP antenna with the gain of 11.8 dBi to downward point to receive reflected GPS signal, a real-time processor unit to perform delay-Doppler mapping of reflected GPS signal as well as log and download raw sampled IF data to the ground for more intensive postprocessing together with a solid state data recorder (SSDR) and high rate downlink (HRD) [14]. Moreover, the processor unit supported to track the direct signal provides the positioning, velocity and timing (PVT). When the receiver was configured as the collection mode, 20 s raw sampled data of the direct and reflected GPS signal could be saved in SSDR to download to the ground.

3.1.2. SGR-ReSI

Following the success of the UK-DMC, SSTL embarked on the new generation spaceborne GNSS-R receiver Space Receiver Remote Sensing Instrument (SGR-ReSI) which had been equipped with UK-TechDemoSat-1 satellite launched in July, 2014 [25]. Compared to the receiver carried on UK-DMC, SGR-ReSI supported to process in real-time and save sampled IF data of multi-frequency GNSS signal. The core component of the receiver is a 24-channel navigation receiver of GPS L1 signal and reprogrammable to a co-processor unit based on Actel ProASIC3 FPGA. The reprogrammable capacity of SGR-ReSI also enables more scientific and remote sensing application. Two types of RF front-ends including Max2769 optimized for GPS L1 signal and Max2112 which is reconfigured to other GNSS bands have been adopted in the receiver. In operation, the receiver could be configured as fixed gain mode (FGM) and unmonitored automatic gain control (uAGC). To allow the storage of both sampled and processed data, a bank of DDR2 memory with a capacity of 1 GB was used. From September 2014 on, the GNSS-R basic observable DDM data formatted as TIFF were downloaded from UK-TechDemoSat-1 to the ground.

3.1.3. GEROS

The main objectives of GEROS mission are to measure the sea surface height and mean square slope, and the secondary ones are to further explore the potential of monitoring vertical profiles of atmospheric using GNSS-RO and to assess the feasibility of GNSS-R for land application [17]. The receiving antenna has 4π steradian field of view capability to receive GNSS signal arriving from any direction and is distinguished into four distinct parts (FoV-1, FoV-2, FoV-3, FoV-4), in which FoV-1 is for altimetry and scatterometry, FoV-2 is for altimetry,

and FoV-3 is for atmosphere/ionosphere sounding. The bandwidth of the GEROS payload is 47 MHz at L1 and 64 MHz at L2 frequency band so that GEROS can perform GNSS-R and GNSS-RO using the signal from different GNSS systems, such as GPS, Galileo, GLONASS, and BeiDou. GEROS can in parallel track three direct and corresponding reflected signals in both RHCP and LHCP at L1 band, only LHCP at L5 band using three antenna beams. The fourth dual-frequency beam could be used to perform either GNSS-R or GNSS-RO. The main Level 1 data of the first three beams are 1 Hz DDM for which the delay and Doppler domain is 1500 m $\times$ 8 KHz and the delay resolution could be configured as 3.75 m and 11.25 m. The fourth beam outputs different Level 1 data depending on the application. GEROS payload has a total mass of 376 kg, a power of 395 W, a 2 GB memory, a 1.2 Mbps output data rate, and the overall dimension of 1.55 m $\times$ 1.17 m $\times$ 0.86 m.

3.1.4. PAU/GNSS-R

Passive Advanced Unit (PAU) is a new instrument concept which aims to monitor ocean parameters. It consists of the PAU/RAD which is an L-band radiometer to measure the brightness temperature of the sea surface, the RAU/GNSS-R which is a reflectometer to measure the roughness of the sea surface and the PAU/IR which is two infrared radiometers used to observe the temperature of the sea surface. PAU/GNSS-R was designed based on FPGA to synchronously process the reflected GPS signal from different satellites in real-time and output corresponding to 2-D DDM [35]. To reduce the hardware resources of the payload, hardware reuse technique was adopted based on two RAM-like registers that change their respective input and output connections to allow the DDM generator to be implemented at a higher clock rate. A software running on MicroBlaze soft processor mainly performs functions including sending and receiving data from the GPS receiver, selecting the available satellites, and computing the DDM parameters transferred to the DDM generator. The computed DDM are transferred to a terminal computer using an USB and an external master based on FPGA.

3.1.5. PYCARO

According to the research and demonstration mission planned by the Remote Sensing Lab and the NanoSat Lab at the Universitat Politècnica de Catalunya-Barcelona Tech, PYCARO will be carried on a 3 $\times$ 2 unit Cube satellite to perform the observation of Earth surface and atmosphere. Compared to the receivers above, the difference of PYCARO is a P(Y) and C/A ReflectOmeter, which adds the processing of encrypted L1 and L2 P(Y) signals by using semicodeless technique [36, 37]. The zenith antenna of PYCARO is a single microstrip patch, and the nadir-looking antenna is a 3 $\times$ 2 array of microstrip patches with 13 dB gain. A dual-channel Software Defined Radio (SDR) is used to sample and collect the signals from the up- and down-looking antennas, and a Gumstix Overo IronStorm OBC manages the payload, configures the SDR, and computes the DDM. PYCARO supports two reconfigurable operation modes including the nadir-pointing mode to perform the Earth surface observation of GNSS-R and the limb-pointing to implement the atmosphere observation GNSS-RO.

3.2. General architecture of receiver

According to the description on the spaceborne GNSS-R receivers above, the general architecture of the receiver could be given as **Figure 6**, which consists of the antennas, the RF front-end, the processor of baseband signal, the computer on-board, and some external components. The antennas include zenith- and nadir-pointing antennas to receive direct and reflected GNSS signal. Usually, the zenith-pointing antenna is an omnidirectional RHCP GNSS antenna, and nadir-pointing antenna is a narrow-beam and high-gain LHCP antenna. However, it is able to be design the different combination of the zenith- and nadir-pointing antennas to perform special spaceborne mission and application. For example, the zenith- and nadir-pointing antennas of PARIS are both the narrow-beam and high-gain antennas to make the incoming signal from the single satellite be received; to significantly measure the soil moisture of the land, the nadir-pointing antenna of GEROS is the combination of the LHCP and RHCP antenna. RF front-ends convert the analog RF signal to the sampled IF one, consisting of Low Noise Amplifier (LNA), bandpass filter, mixer, gain control, and A/D converter. According to the requirement of the mission, the gain control could have different configuration. For altimetry, the Automatic Gain Control (AGC) mode is utilized to dynamically adjust the power level of incoming signal to the most effective input range of A/D converter; however, the scatterometry of GNSS-R generally selects the fixed gain or monitoring AGC to correctly receiving gain to obtain accuracy power level of reflected signal. To improve the generality of the receiver, the gain control could be designed as reconfigurable mode, such as SGR-ReSI of which the gain control supports the fixed gain and unmonitoring AGC mode. The core of the receiver is a baseband processor which consists of controller and processor unit. The controller unit controls the acquirement

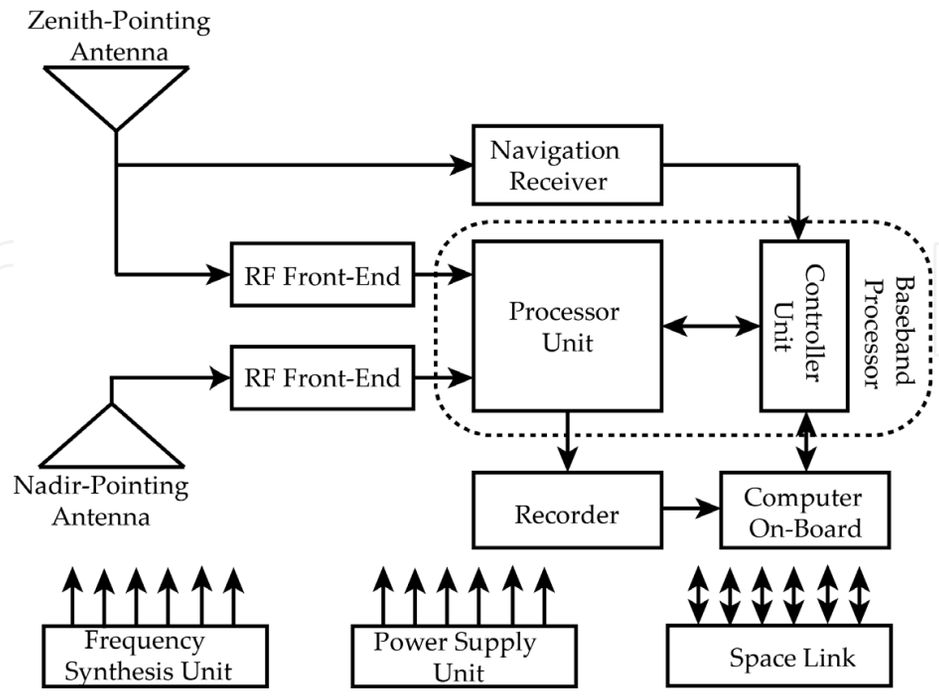

Figure 6. Architecture of Spaceborne GNSS-R receiver.

and tracking of direct signal, estimates the difference of delay and Doppler frequency between direct and reflected signal, and configures the DDM parameters, such as delay and Doppler frequency window range and resolution and others. The estimations of the differences of delay and Doppler frequency between direct and reflected signal are given as

$$\Delta\tau = \frac{|\mathbf{T}-\mathbf{S}| + |\mathbf{R}-\mathbf{S}| - |\mathbf{T}-\mathbf{R}|}{c} \tag{17}$$

$$\Delta f = \frac{\mathbf{v}_r \cdot \mathbf{u}_{rs} - \mathbf{v}_t \cdot \mathbf{u}_{ts} - (\mathbf{v}_t \cdot - \mathbf{v}_r) \cdot \mathbf{u}_{tr}}{\lambda} \tag{18}$$

where $\mathbf{T}$ and $\mathbf{v}_t$ are the positioning and velocity of GNSS satellite; $\mathbf{R}$ and $\mathbf{v}_r$ are the positioning and velocity of LEO satellite; $\mathbf{S}$ is the positioning of the specular point; $\mathbf{u}_{rs}$ and $\mathbf{u}_{ts}$ are the unit vectors from LEO and GNSS satellite to the specular point; $\mathbf{u}_{tr}$ is the unit vector from the LEO to GNSS satellite; c is the speed of light; and λ is the wavelength of GNSS signal. To make the DDM in the window of delay and Doppler frequency, it is necessary to provide high-accuracy positioning and velocity of GNSS, LEO satellite and specular point to meet the estimated accuracy of expression (17) and (18). The processor unit performs the auto/cross-correlation operation, in which the auto-correlation mode correlates the reflected signal with locally generated replicas at the different delay and Doppler frequency, and the cross-correlation mode correlates the reflected signal with the direct signal after proper delay and Doppler adjustment. Compared to the auto-correlation mode, the cross-correlation mode overcomes the bandwidth limitation to improve the range resolution and decreases the computational complexity. However, the main shortcoming of the cross-correlation is that the large-size and narrow-beam antennas are required for both direct and reflected signal to separate signal from different satellites. To overcome the bandwidth limitation and decrease the antenna size, a new approach is to use semicodeless technique to locally reconstruct encrypted P(Y) code and then cross-correlate them with reflected signal. The computer on-board performs the control and management of satellite mission to receive and route ground commands for the configuration of the DDM parameters and the operation modes, assemble and packet useful data for downloading to the ground. External components include power supply unit, frequency synthesis unit and space link to provide the required power supplies, working clocks for the units of the whole system, and the spatial interface linking the satellite and ground station.

3.3. Processing method

At present, the processing methods of reflected GNSS signal have serial and parallel correlation. The serial correlation correlates the reflected GNSS signal with the locally generated replicas at the different delay and Doppler frequency one by one in time domain. The parallel correlation first transforms the reflected and local signal to the frequency domain using fast Fourier transform (FFT) and performs a multiplication operation, then transforms multiple results to time domain using Inverse FFT (IFFT). The serial processing is lossless and can be considered as the

reference for the assessments of parallel method. The assessment metric is defined as normalized mean squared error (MSE) between serial and parallel correlation as

$$\sigma^2 = \frac{\sum_{i=1}^{N_\tau}\sum_{j=1}^{N_f}\left|\left\langle\left|Y_S\left(\tau_i,f_j\right)\right|^2\right\rangle - \left\langle\left|Y_P\left(\tau_i,f_j\right)\right|^2\right\rangle\right|^2}{\sum_{i=1}^{N_\tau}\sum_{j=1}^{N_f}\left|\left\langle\left|Y_S\left(\tau_i,f_j\right)\right|^2\right\rangle\right|^2} \tag{19}$$

where $\left\langle\left|Y_S\left(\tau_i,f_j\right)\right|^2\right\rangle$ and $\left\langle\left|Y_P\left(\tau_i,f_j\right)\right|^2\right\rangle$ are the mean correlation power computed by serial and parallel method when the delay and Doppler frequency of local replica are τ_i and f_j; N_τ and N_f are the number of delay and Doppler bin.

3.3.1. Serial correlation

Serial correlation in time domain is expressed as

$$Y_S\left(\tau_i,f_j\right) = \frac{1}{N_S}\sum_{i=1}^{N_S} u_r(t)p(t-\tau)\exp\left\{-2\pi j\left(f_0+f_j\right)t\right\} \tag{20}$$

where N_S is the sampling number in a GNSS-code period. The block diagram of the serial processing is shown in **Figure 7**, in which the channel is $N_\tau \times N_f$. Each channel requires multiplier $3N_S$ and adder $2N_S$. The total numbers of the multipler and the adder are $3N_SN_\tau N_f$ and $2N_SN_\tau N_f$, respectively.

3.3.2. Parallel correlation in delay domain

Parallel correlation in delay domain parallelly performs correlation operation for all code delay based on Fourier transform in each Doppler channel as

$$Y_P\left(:,f_j\right) = \mathrm{IFFT}\left\{\mathrm{FFT}\left\{u_r(t)\exp\left(-2\pi j\left(f_0+f_j\right)\right)\right\}\{\mathrm{FFT}\{p(t)\}\}^*\right\} \tag{21}$$

where FFT{·} and IFFT{·} respresent the FFT and IFFT operator; and $\{\cdot\}^*$ is the conjugate operator. **Figure 8** is the block diagram of the parallel correlation in delay domain. The number of the processing channel is N_f. As it is known, FFT operation with N_S sampled ponits requires multipler and adder $2N_S\log_2 N_S$ and $3N_S\log_2 N_S$. From **Figure 8**, it is seen that each channel performs 2 FFT and 1 IFFT with N_S sampled ponits. The total numbers of the required multipler and adder are $6N_fN_S\log_2 N_S$ and $9N_fN_S\log_2 N_S$, respectively.

3.3.3. Parallel correlation in Doppler domain

Parallel correlation in Doppler domain performs spectrum estimation for the signal removed the modulation of the code at each delay channel as

$$Y_P(\tau_i,:) = \mathrm{FFT}\{u_r(t)p(t-\tau)\exp\{-2\pi j f_0 t\}\} \tag{22}$$

The block diagram is illustrated as in **Figure 9**, in which the number of processing channel is N_τ. In each channel, correlation operation is divided into two steps: decimation and spectrum estimation. To prevent the overlapping of the spectrum, it is necessary to add an anti-aliasing filter before resampling. In engineering, one of the most efficient anti-aliasing filters is Cascaded Integrator Comb (CIC) filter which requires adder about $2N_S$. The spectrum of decimated signal is estimated using FFT, which needs multipler and adder

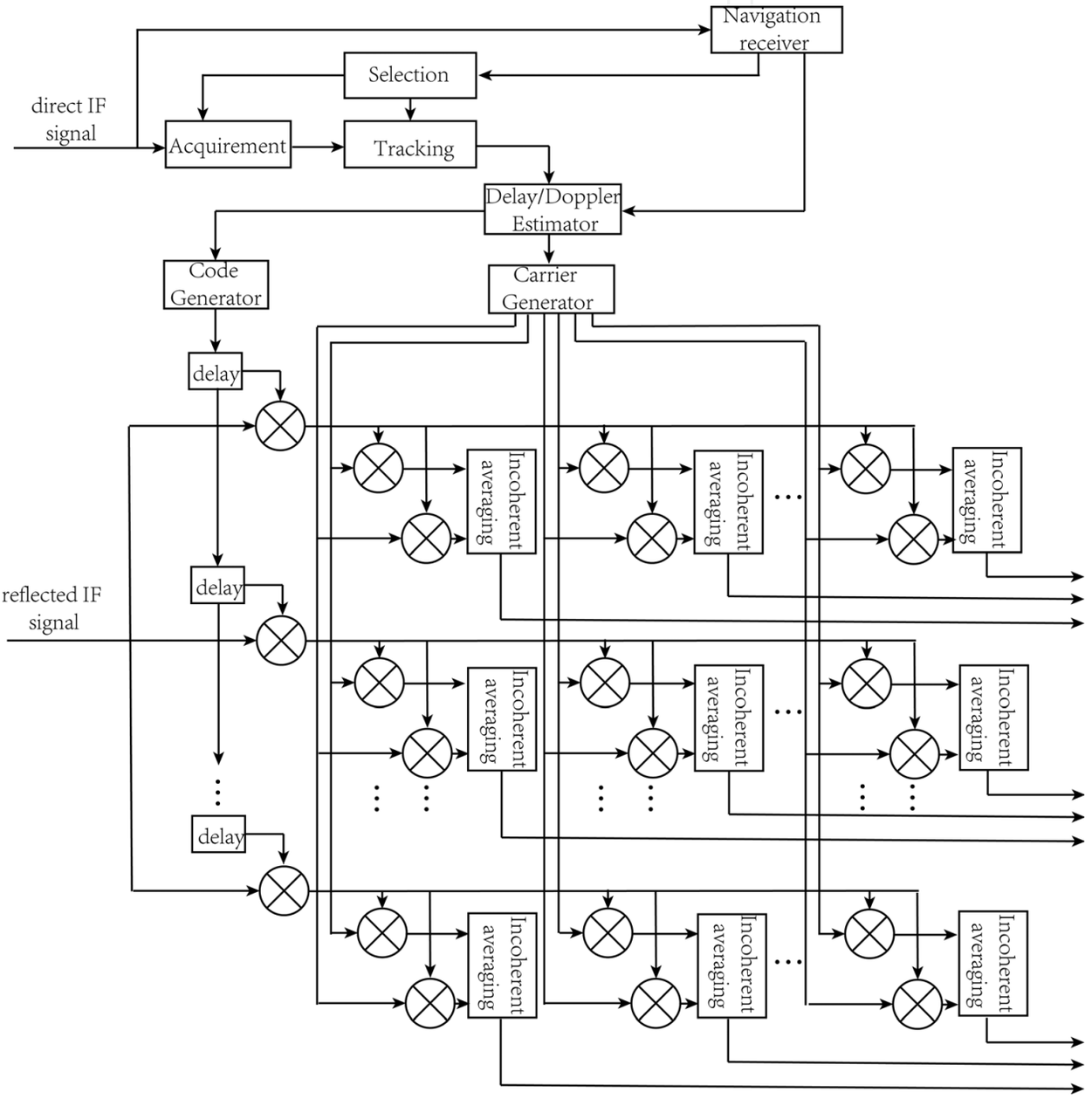

Figure 7. Block diagram of serial correlation method.

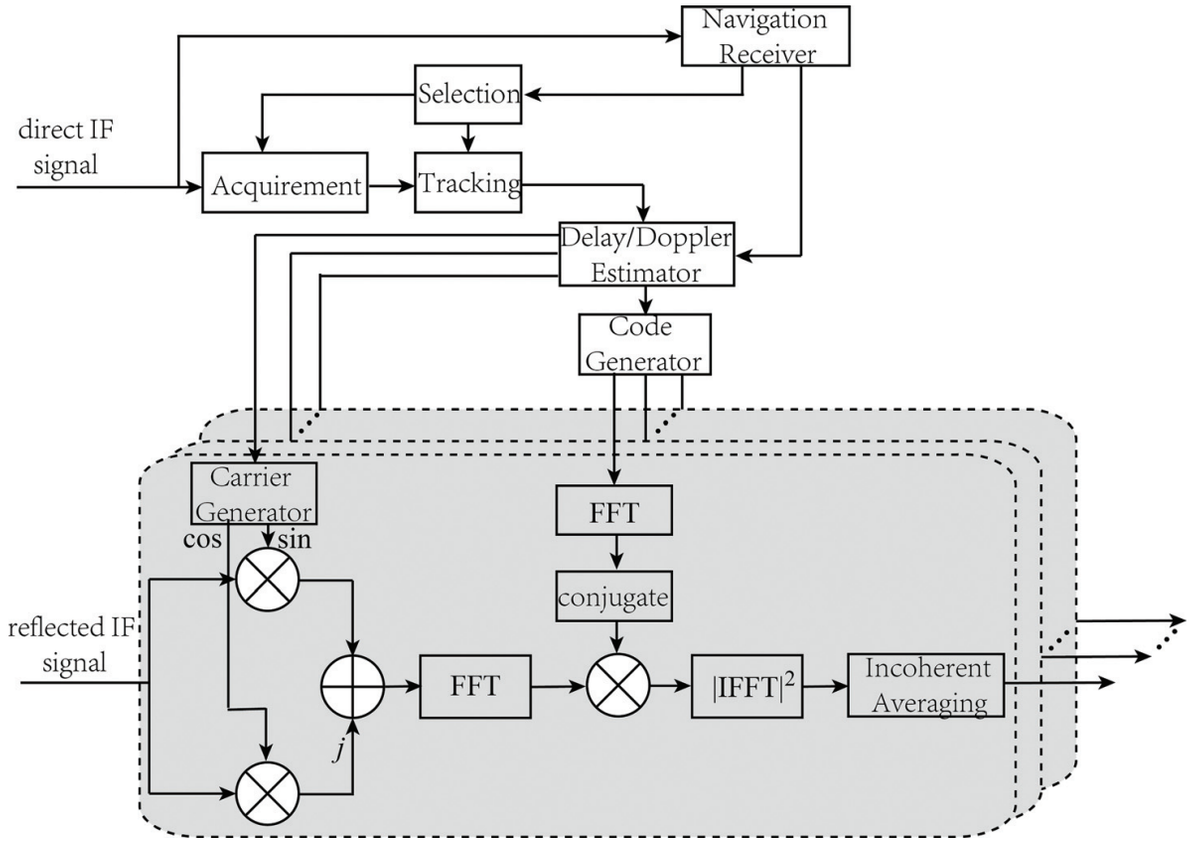

Figure 8. Block diagram of parallel correlation in delay domain.

about $2N_f\log_2 N_f$ and $3N_f\log_2 N_f$. The total numbers of the multipler and adder are $2N_\tau N_f\log_2 N_f$ and $N_\tau\left(3N_f\log_2 N_f + 2N_S\right)$.

3.3.4. Parallel correlation in delay-Doppler domain

Parallel correlation in delay-Doppler domain [38], as given in **Figure 10**, is a block processing technique called as double-block zero-padding (DBZP) expressed as

$$Y_P(:,:) = \mathrm{FFT_c}\left\{\begin{array}{c} A_1 \\ A_2 \\ \vdots \\ A_{N_b} \end{array}\right\} \tag{23}$$

$$A_i = \mathrm{IFFT_r}\{\mathrm{FFT_r}\{[U_i, U_{i+1}]\}\cdot\{\mathrm{IFFT_r}[P_i, \mathbf{0}]\}^*\} \tag{24}$$

where U_i and P_i are the ith blocks of the reflected signal and local replica; $\mathbf{0}$ is the zero vector; $\mathrm{FFT_r}\{\cdot\}$ and $\mathrm{IFFT_r}\{\cdot\}$ respresent FFT and IFFT operation for the row of the matrix; and $\mathrm{FFT_c}\{\cdot\}$ is FFT operation for the column of the matrix. Expression (23) is the parallel correlation in delay domain for the block, and expression (24) could be considered as the spectrum estimation. To simplify the analysis of the computational complexity, it is assumed that $N_b = N_f/2$

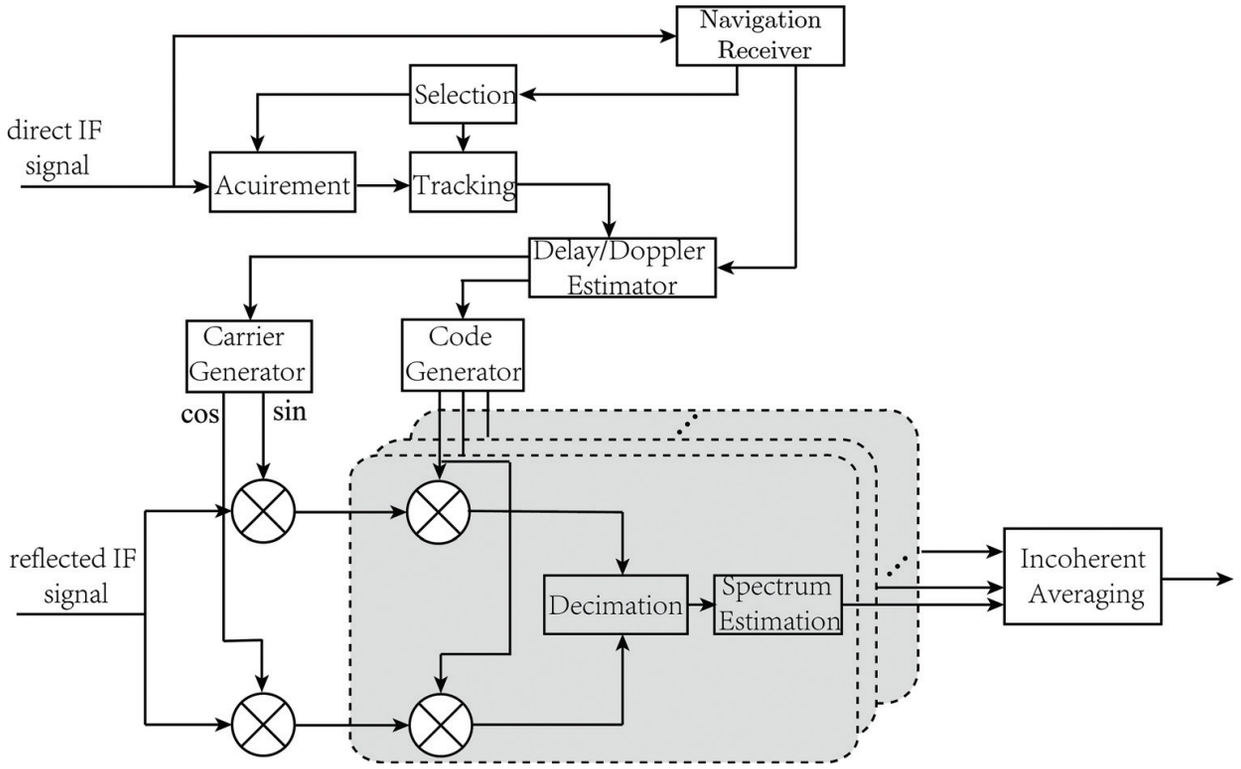

Figure 9. Block diagram of parallel in Doppler domain.

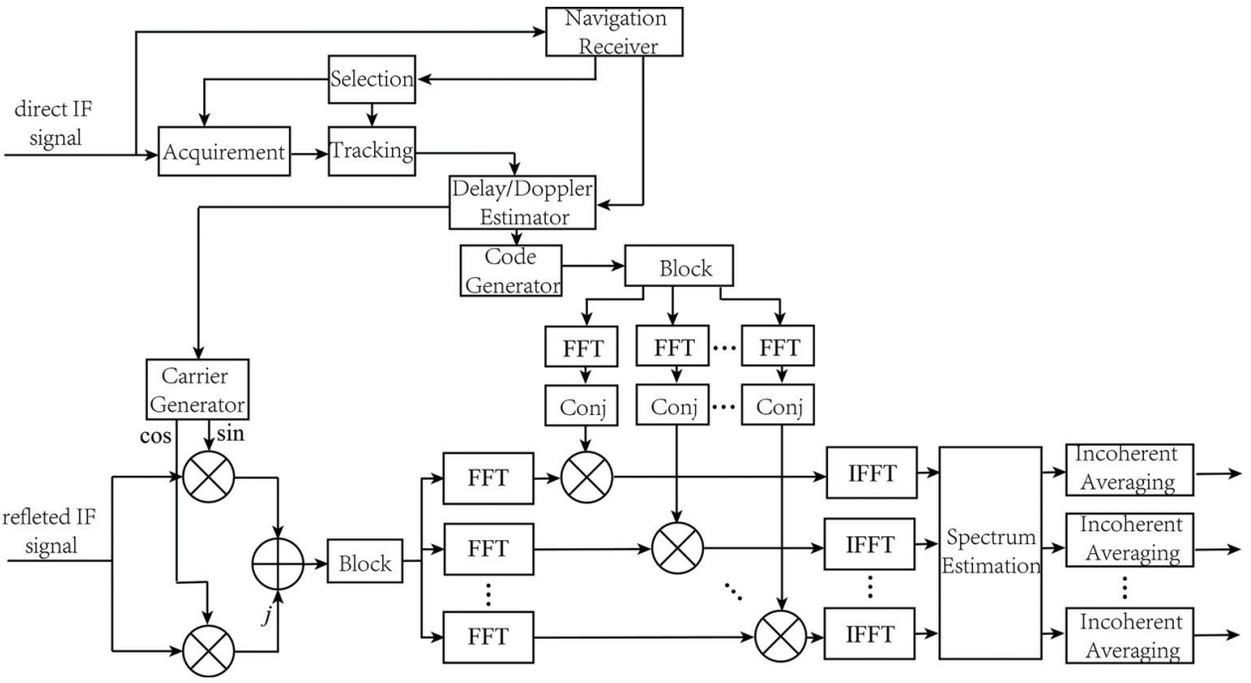

Figure 10. Block diagram of parallel correlation in delay-Doppler domain.

and the element number of the block N is $\lceil 2N_s/N_f \rceil$ ($\lceil\cdot\rceil$ is rounding operator). The numbers of the multipler and adder for each block is $12N\log_2 2N$ and $18N\log_2 2N$. The numbers of multiplier and adder required by the spectrum estimation are $4N_b\log_2 2N_b$ and $6N_b\log_2 2N_b$. The total numbers of multipler and adder for DBZP are $12N_bN\log_2 2N + 2N_f\log_2 N_f$ and $18N_bN\log_2 2N + 3N_f\log_2 N_f$.

3.3.5. Comparison of computational complexity

Although the computational complexities of the correlation processing have been analyzed above, here, the simulated comparison is conducted. It is assumed that the range and the resolution of Doppler frequency are [−8, 8] KHz and 500 Hz, respectively, and the numbers of delay bin and the DBZP block are same. **Figure 11** gives the simulated computational complexities when the numbers of the sampling are 2048, 4096, 8192, and 16,384, from which it is seen that (1) serial correlation needs most multiplier and adder and consumes most hardware resources so that it is unsuitable for spaceborne receiver; (2) parallel correlation methods significantly reduce the number of required multiplier and adder, especially parallel correlation in Doppler domain. It should be noted FFT and IFFT on hardware is a 2-based operation which needs to padding zero to make the number of operating point to be the power of 2. Large number of padding zero causes the increasing of computational complexity; therefore, it has to be considered to choose optimal DDM parameters.

3.4. Processing of UK-TDS/UK-TDS-1 data

The raw IF data from UK-DMC and UK-TechDemoSat-1 satellite are used to demonstrate the correlation approaches above. UK-DMC satellite which first carried an experimental GNSS reflectometry aimed to monitor the disaster using optical imaging. In 2003, UK-DMC satellite was launched into the sun-synchronous orbit with 680 km altitude. Some

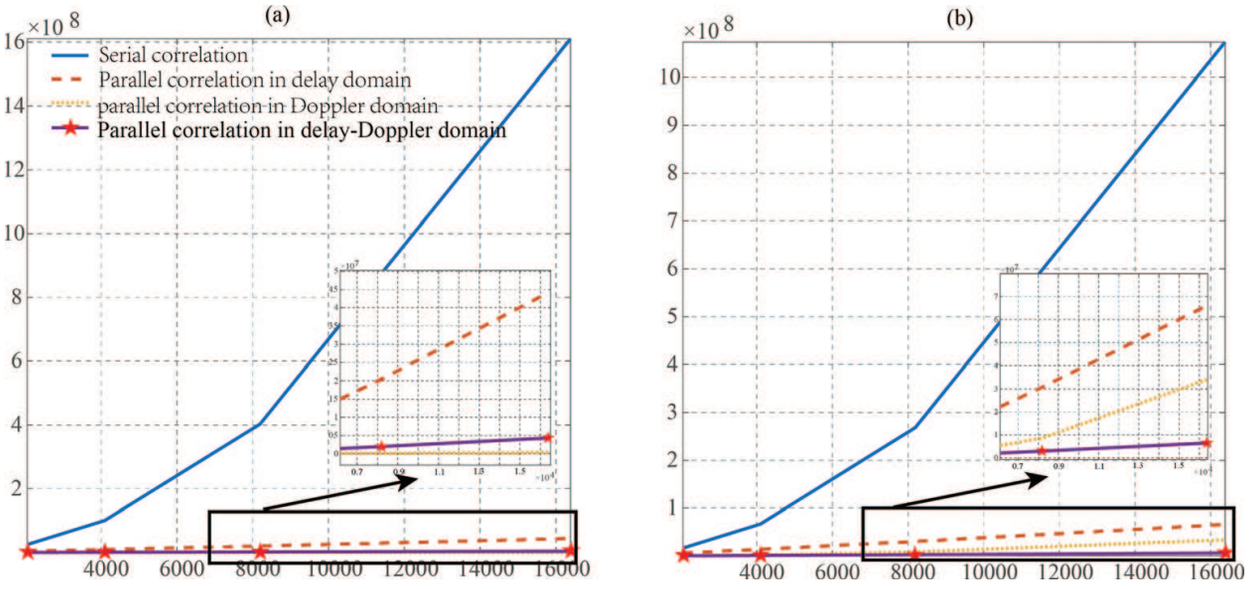

Figure 11. Simulated number of multiplier and adder required correlation processing.

researchers have used GNSS-R data from UK-DMC satellite to demonstrate the feasibility of remotely sensing sea wind speed, sea ice, and others. Following the end of UK-DMC's operational life in 2011, SSTL launched UK-TDS-1 satellite equipped with new generation spaceborne GNSS-R receiver SGR-ReSI in 2014. The orbit of UK-TDS-1 satellite is also sun-synchronous orbit with the altitude and the inclination of 635 km and 98.4°, respectively. UK-TDS-1 satellite is controlled and operated with a 8-day duty circle shared between 8 payloads. SGR-ReSI can be operated for only 2 days in every 8-day period. Both UK-DMC and UK-TDS-1 satellite support the collection of raw IF data, however, because of the limitation of the storage capacity, only a few raw IF data are available. Here, the data collected by UK-DMC on November 11, 2004 and UK-TDS-1 on January 27, 2015 are used. The corresponding ground track of GNSS, UK-DMC, and UK-TDS-1 satellite, and the positioning of the specular pointing are shown in **Figure 12**, in which both specular pointings lie to the ocean surface, i.e., the signals collected by UK-DMC and UK-TDS-1 satellite are both reflected from the ocean surface. **Figure 13** shows the DDM distribution of reflected GNSS signal collected by UK-DMC and UK-TDS-1 satellite, in which from left to right, the DDMs are computed using serial correlation, parallel correlation in delay domain, parallel correlation in Doppler domain, and parallel correlation in delay-Doppler domain. From **Figure 13**, it could be seen that (1) the DDMs from UK-DMC and UK-TDS-1 satellites both show the distribution of the horseshoe shape as simulated in **Figure 4** of Section 2.3; (2) the DDMs computed by four correlation methods have similar distribution in delay-Doppler domain. The assessment metrics defined by expression (19) are computed for the DDMs in **Figure 13**. The results are given in **Table 1**, which indicate that compared to the serial correlation, parallel correlations have negligible MSEs, and in addition, one-dimensional parallel methods have lower MSEs than two-dimensional ones. The results above illustrate that parallel correlations, especially the parallel correlation in Doppler domain, are better chosen to compute the DDM than serial one for spaceborne GNSS-R receiver.

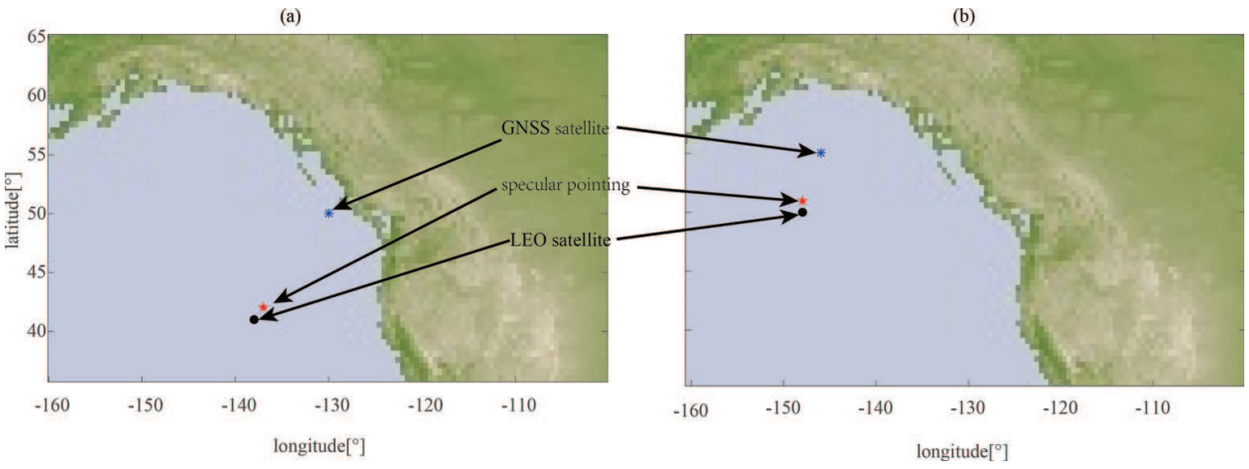

Figure 12. Ground track of satellites and the positioning of the specular pointing when (a) UK-DMC and (b) UK-TDS-1 data were collected.

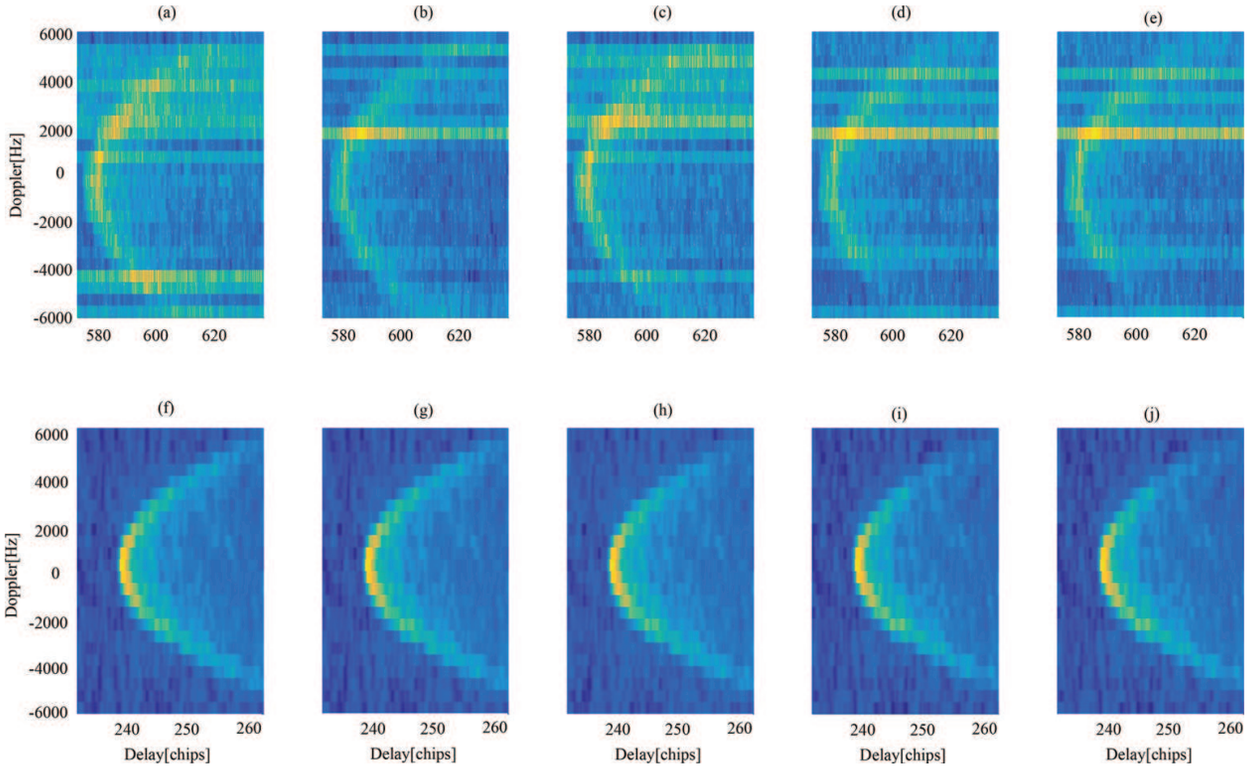

Figure 13. DDM of (a)–(e) UK-DMC and (f)–(j) UK-TDS-1 data.

Satellite	Serial	Parallel ($\times 10^{-3}$)		
		Delay domain	**Doppler domain**	**Delay-Doppler domain**
UK-DMC	0	5.81	2.62	6.94
UK-TDS-1	0	0.09	0.32	1.17

Table 1. Comparison of normalized MSE between correlation powers obtained by serial and parallel processing.

4. Retrieving of wind speed

Retrieving wind speed is an inversion problem of remote sensing, of which the key is to find and extract the sensitivity parameters to wind speed from the basic observables of the remote sensing sensors. In fact, L-band signals are less optimal frequency for the measurement of wind speed compared to scatterometers, however, are not significantly attenuated by rainfall so that they are available to observe wind speed in tropical cyclones. As mentioned in Section 1, at present, three types of retrieving approaches for spaceborne GNSS-R have been proposed. Here, the approaches based on the direct mapping from DDM metrics to wind speed are discussed.

4.1. Retrieving method

An expression for the distribution of DDM in delay-Doppler domain has been given in (15), in which the parameter related to sea wind speed is bi-static scattering coefficient σ_0^2. Therefore, it is able to observe wind speed using bi-static scattering coefficient derived from the DDM. As bi-static scattering coefficient is ununiform over the sea surface, the integrated area used in calculating bi-static scattering coefficient should be chosen to optimize the accuracy of calculation. The ideal area in which bi-static scattering coefficient could be assumed as the constant is a small region around the specular point. The corresponding power which usually is nearby the peak DDM is expressed as [30, 39]

$$\left\langle \left| Y\left(\widehat{\tau},\widehat{f}\right)\right|^2 \right\rangle = A_R^2 T_I^2 \sigma_0^2 \iint \frac{G^2(\boldsymbol{\rho})\Lambda^2(\widehat{\tau}-\tau(\boldsymbol{\rho}))\cdot \mathrm{sinc}^2\left(\widehat{f}-f(\boldsymbol{\rho})\right)}{4\pi D(\boldsymbol{\rho})^2 d(\boldsymbol{\rho})^2} d^2\boldsymbol{\rho} \tag{25}$$

The expression computing bi-static scattering coefficient is derived as

$$\sigma_0^2 = \frac{\left\langle \left| Y\left(\widehat{\tau},\widehat{f}\right)\right|^2 \right\rangle}{\left[A_R^2 T_I^2 \iint \frac{G^2(\boldsymbol{\rho})\Lambda^2\left(\widehat{\tau}-\tau(\boldsymbol{\rho})\right)\cdot \mathrm{sinc}^2\left(\widehat{f}-f(\boldsymbol{\rho})\right)}{4\pi D(\boldsymbol{\rho})^2 d(\boldsymbol{\rho})^2} d^2\boldsymbol{\rho}\right]} \tag{26}$$

In expression (26), A_R is an unknown parameter related to the transmit power and antenna gain of GNSS satellite, the atmospheric loss. Generally, direct signal and some atmospheric attenuation models are used to estimate it. In addition, the integral operation in expression (26) is time-consuming; therefore, the expression (26) is further simplified by assuming the changes of $G(\boldsymbol{\rho})$, $\tau(\boldsymbol{\rho})$, and $f(\boldsymbol{\rho})$ in the small region around the specular pointings as unity. The simplified expression of σ_0^2 could be given as

$$\widehat{\sigma}_0^2 = \frac{4\pi D^2 d^2 \left\langle \left| Y\left(\widehat{\tau},\widehat{f}\right)\right|^2 \right\rangle}{A_R^2 T_I^2 G_{\mathrm{SP}} A_0} \tag{27}$$

where G_{SP} is the gain of the nadir-looking antenna at the specular point; and A_0 is the size of scattering area around the specular point. To reduce the influence of the noise, $\left\langle \left| Y\left(\widehat{\tau},\widehat{f}\right)\right|^2 \right\rangle$ in expressions (26) and (27) could be replaced by the averaged DDM around the peak as

$$P_{\mathrm{avg}} = \frac{1}{MN}\sum_{i=1}^{M}\sum_{j=1}^{N}\left\langle \left| Y\left(\tau_i, f_j\right)\right|^2 \right\rangle \tag{28}$$

As illustrated in **Figure 5**, the DDM not only gives the distribution of correlation power in delay-Doppler domain, but also presents the spatial distribution of power. The given

delay-Doppler interval in expression (28) determines the geometric resolution of spaceborne GNSS-R as [40]

$$R_{\text{geo}} = \sqrt{\int \Pi\left(\frac{\tau(\boldsymbol{\rho}) - \tau_L/2}{\tau_L}\right) \cdot \Pi\left(\frac{f(\boldsymbol{\rho})}{2f_M}\right) d\boldsymbol{\rho}} \tag{29}$$

where τ_L and f_M are the maximum delay and Doppler frequency in expression (28).

4.2. Demonstration of UK-TDS-1 and ASCAT data

The gain modes of RF front-end in SGR-ReSI have unmonitoring AGC and fixed gain. After June 2015, SGR-ReSI was configured as the fixed gain of 36 dB. The UK-TDS-1 Level 1 data collected from November 26, 2015 to April 19, 2016 are used to demonstrate the feasibility of retrieving wind speed using the approach above. Wind speed monitored by ASCAT-A/B which have a resolution of 25 km are selected as in-situ data. The matchup between the specular pointing of UK-TDS-1 and the ground track of ASCAT-A/B are set to allow a maximum space and time separation of 0.25° and 1 h. To improve the accuracy of retrieved wind speed, it is necessary to select high-quality L1 data to retrieve wind speed. The first is spatial selection that the latitude range of the specular point is limited from −50°S to −50°N to remove the data reflected off the sea ice, and the distances between the specular pointing and the coastline are controlled to be over 0.5° to remove the impact of the land on the DDM. The second one is the selection based on the antenna gain at the specular point. The nadir-looking antenna gains of SGR-ReSI rapidly attenuate when the incident angles of incoming signal are over 40°. Therefore, the incident angles of GNSS signal are limited within the range of 30°. The reflected GNSS signal arriving at the nadir-pointing antenna is exceedingly weak. The coherent integration of 1 ms and incoherent averaging of 1000 significantly improve the signal-to-noise ratio (SNR); however, some DDMs still are buried in the noise floor. In addition, the SNR is one of the factors influencing on the accuracy of wind speed. Therefore, it is needed to remove DDMs with the low SNR. The SNR of DDM could be defined as

$$\text{SNR} = \frac{P_{\text{peak}}}{N_{\text{floor}}} - 1 \tag{30}$$

where P_{peak} is the peak DDM; and N_{floor} is the noise floor of DDM, which can be computed by averaging the DDM in the region where reflected signal is absent.

After the DDMs are selected, the delay and Doppler interval in expression (28) should be determined. The delay and Doppler interval are limited by the geometric resolution. **Figure 14** shows the relationship between the geometric resolution and the incident angle for different delay interval when Doppler interval is [−1, 1] KHz, from which it is seen that when delay interval is [−0.25, 0.25] chips, the geometric resolution is lower than 25 km which is required resolution of the traditional spaceborne remote sensing. Based on the discussion, the delay and Doppler interval in expression (28) are configured as [−0.25, 0.25] chips and [−1, 1] KHz.

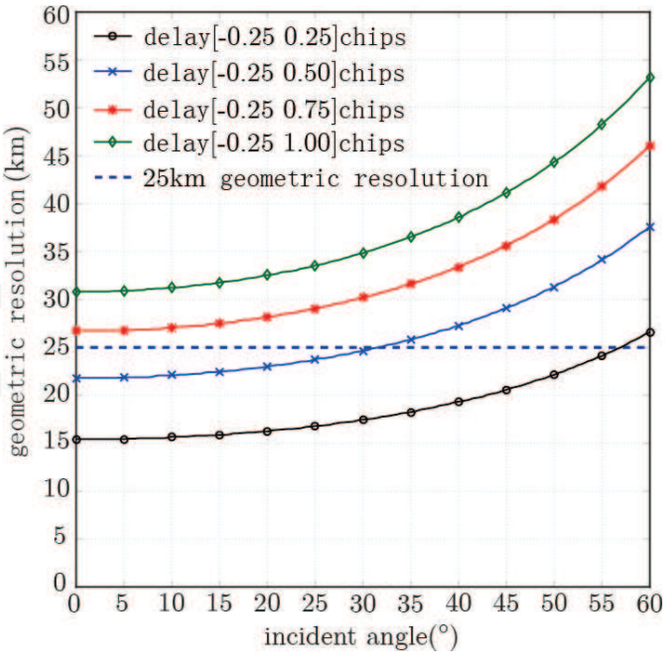

Figure 14. Relationship between geometric resolution and incident angle.

The retrieval model is the mapping linking wind speed with the bi-static scattering coefficient computed by expression (26) or (27). Note that because of the unknown transmit power and antenna gain, the influence of A_R^2 on the bi-static scattering coefficient ignored by assuming them as the constants. Moreover, when the incident angle of GNSS signal is lower than 35°, $1/\cos^2\theta$ could be used to replace A_0 in the expression (27) because of the proportional relationship between them [41]. Therefore, the observable used to develop the link with wind speed is not a true bi-static scattering coefficient. The selected data are divided into two groups: train and test set. The relationship between the observable and wind speed is fitted as

$$U_{10} = Ae^{B\sigma_{\text{obs}}^2} + C \tag{31}$$

where σ_{obs}^2 is the obervable computed by expressions (26) and (27) when A_R^2 are ignored and A_0 is replaced using $1/\cos^2\theta$; and A, B, and C are fitted parameters. **Figure 15** shows the inversely proportional relationship between the observable computed by expressions (26) and (27) and wind speed. The fitted parameters in expression (31) are obtained by fitting the observables of train set with wind speed measured by ASCAT-A/B. The compared results between ASCAT-A/B-retrieved wind speed using test set are presented in **Figure 16** and **Table 2**. The biases between ASCAT-A/B and retrieved wind speed are ignorable, 0.024 m/s and 0.021 m/s, for the observables derived by expressions (26) and (27). The RMSEs are 2.11 m/s and 2.15 m/s, respectively. In addition, it is clear that the retrieving accuracy for high wind speed is larger than the low wind speed as illustrated in **Figure 17**, in which when wind speed is lower than 11 m/s, the RMSE is less than 2 m/s. The reasons of bad RMSE for high wind speed are that (1) the low percentage of high wind speed in train set causes the poor fitting of expression (31); and (2) the sensitivity of the observable on wind speed decreases as wind speed increases. Moreover, it is pointed that the approach based on the expression (27) can take less time about 3000 times than the approach based on the expression (26).

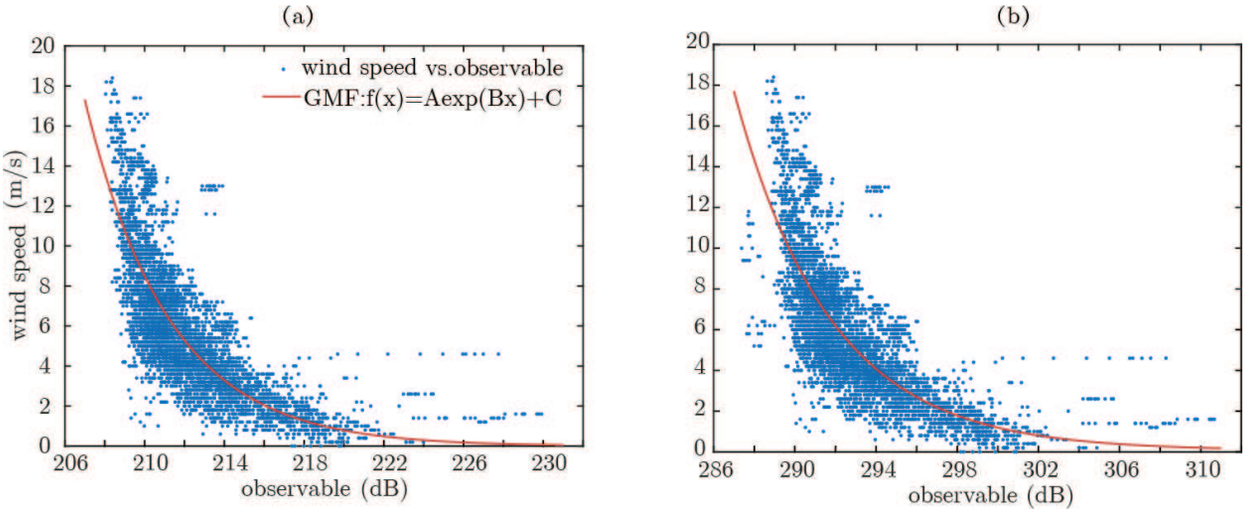

Figure 15. Scatter plot of observable computed by expression (a) (26) and (b) (27) vs. wind speed.

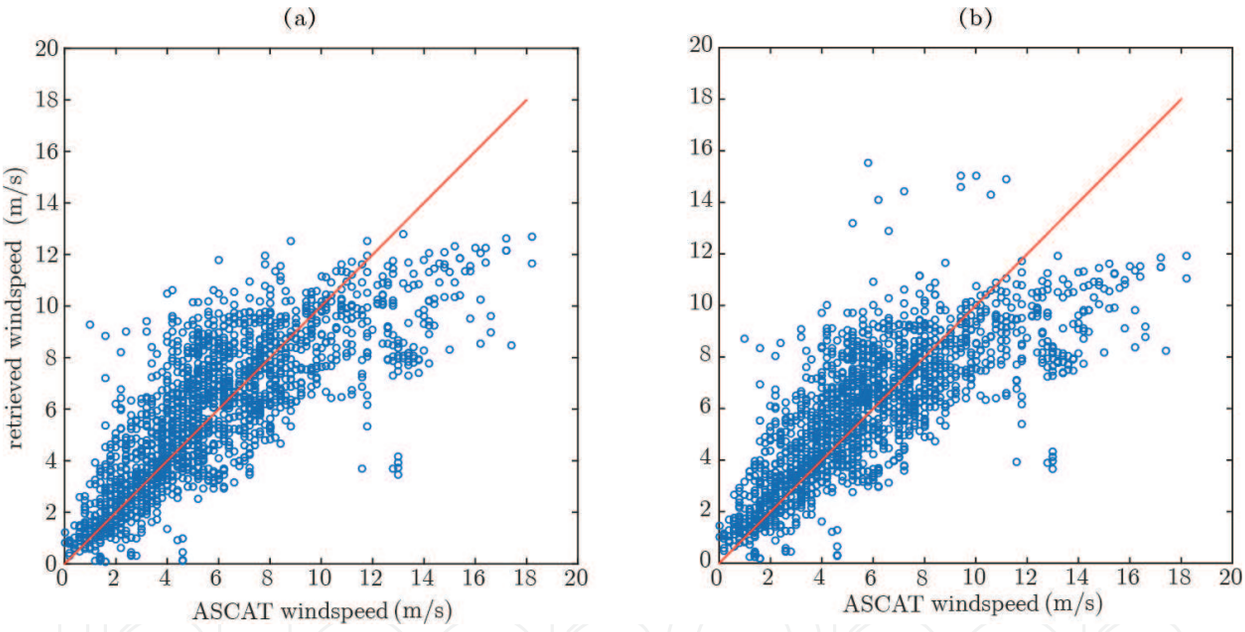

Figure 16. Scatter plot of ASCAT-A/B and retrieved wind speed.

Observable	Train set			Test set	
	A	B	C	Bias (m/s)	RMSE (m/s)
Expression (26)	3.506×10^{22}	−0.237	−0.0115	0.024	2.11
Expression (27)	4.299×10^{27}	−0.2177	−0.0665	0.021	2.15

Table 2. Trained parameters of Eq. (31) using train set and corresponding test performance using test set.

The SNR of DDM has an important impact on retrieving result of wind speed as shown in **Figure 18**. The accuracy of retrieved wind speed is improved by selecting the DDMs with higher SNR. However, it should be noted that the larger the threshold of the SNR is, the lesser

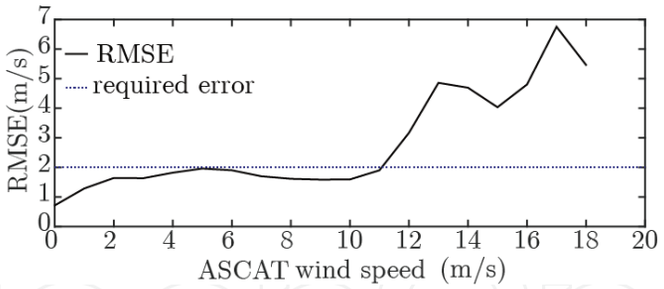

Figure 17. Relationship of RMSE of retrieved wind speed vs. wind speed.

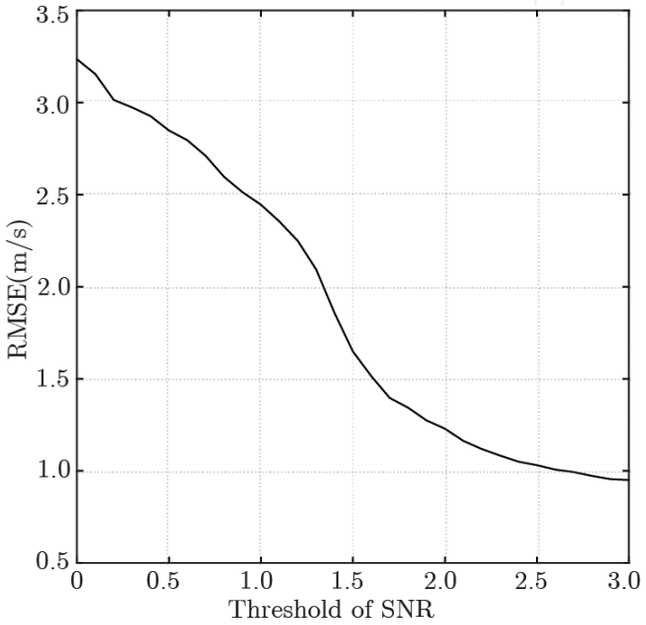

Figure 18. Trend plot of RMSE as the threshold of SNR changing.

the DDMs used to the retrieved wind speed are, i.e., the coverage of the UK-TDS-1 is lower for the higher threshold of the SNR. It has to be noted that no precise calibration and correction for the DDM measurement in SGR-ReSI also is one of the reasons causing the low performance of retrieving wind speed.

5. Conclusion

GNSS-R has been a new tool of remote sensing to monitor Earth's physical parameters, such as sea wind speed, sea surface height, sea ice, soil moisture and others. Following the success of UK-DMC satellite which was carried on the first GNSS-R receiver, the spaceborne GNSS-R which could provide the global and all-days observation has been an hot focus of the research groups. Some spaceborne missions have been proposed and planned, such as CYGNSS of NASA, GEROS-ISS of ESA, ^{3}CAT-2 of the Remote Sensing Lab and the NanoSat Lab at the universitat Politècnica de Catalunya-Barcelona Tech. This chapter was focused on the discussion of spaceborne GNSS-R to monitor sea wind speed. First, the basic theories

of spaceborne GNSS-R, including the geometry, polarization, and scattering model were discussed. The geometry of GNSS-R mainly is determined by the incident angle of GNSS signal, and the height of LEO and GNSS satellite. When GNSS signal occurs reflection on the sea surface, the polarization of GNSS signal is changed. At nadir and small incident angle, the LCHP component dominates the reflected GNSS signal. For the diffuse scattering of the GNSS signal, the correlation power level called as DDM spreads to large delay and Doppler frequency and presents the horseshoe shape in delay-Doppler domain. Then, the spaceborne receivers and processing methods were discussed. The results showed that parallel correlation in Doppler domain has lowest computational complexity and optimal performance so that it is optimal to choose to process the reflected GNSS signal in real-time for spaceborne receiver. Finally, the approach based on DDM metric was used to retrieve wind speed. Proposed DDM metrics have inversely proportional relationship with wind speed. By latitude mask and the threshold of SNR to remove low-quality data, proposed approaches could obtain the RMSE of 2.11 m/s and 2.15 m/s. For further improvement of retrieving accuracy, it is necessary to set higher SNR threshold which results in lower spatial coverage. In one word, GNSS-R will become an effective way to observe global sea wind speed, especially low attenuation of GNSS signal for the rainfall will be an optimal choice to monitor tropical cyclone.

Author details

Dongkai Yang* and Feng Wang

*Address all correspondence to: wangf.19@163.com

School of Electronic and Information Engineering, Beihang University, Beijing, China

References

[1] Adler RF. Estimating the benefit of TRMM tropical cyclone data in saving lives. In: American Meteorological Society, 15th Conference on Applied Climatology; 2005; Savannah, USA

[2] Draper DW, Mccabe PJ. A review of satellite altimeter measurement of sea surface wind speed: With a proposed new algorithm. Journal of Geophysical Research. 1985;**90**(C3): 4707-4720. DOI: 10.1029/JC090iC03p04707

[3] Stoffelen A, Anderson DLT. Wind retrieval and ERS-1 scatterometer radar backscater measurements. Advances in Space Research. 1993;**13**(5):53-60. DOI: 10.1016/0273-1177(93)90527-I

[4] Chang PS, Li L. Ocean surface wind speed and direction retrievals from the SSM/I. IEEE Transactions on Geoscience and Remote Sensing. 1998;**36**(6):1866-1871. DOI: 10.1109/36.729357

[5] Komkathy A, Armatys M, Masters D, Axelrad P, Zavorotny VU, Katzberg SJ. Retrieval of ocean wind speed and wind direction using reflected GPS signals. Journal of Atmospheric and Oceanic Technology. 2004;**21**(3):515-526

[6] Lowe ST, Zuffada C, Chao Y, Kroger P, et al. 5-cm precision aircraft ocean altimetry using GPS reflections. Journal of Geophysical Research. 2002;**29**(10):13(1)-13(4). DOI: 10.1029/2002GL0-14759

[7] Rivas MB, Maslanik JA, Axelrad P. Bistatic scattering of GPS signals off Arctic sea ice. IEEE Transactions on Geoscience and Remote Sensing. 2009;**48**(3):1548-1553. DOI: 10.1109/TGRS.2009.2029342

[8] Katzberg SJ, Torres O, Grant MS, Masters D. Utilizing calibrated GPS reflected signals to estimate soil reflectivity and dielectric constant: Results from SMEX02. Remote Sensing of Environment. 2005;**100**(1):17-28. DOI: 10.1016/j.rse.2005.09.015

[9] Hall C, Cordy R. Multistatic scatterometry. In: Proc. IEEE Int. Geoscience Remote Sensing Symp; 1988; Edinburgh, Scotland

[10] Martin-Neira M. A passive reflectometry and interferometry system (PARIS): Application to ocean altimetry. ESA Journal. 1993;**17**(4):331-355

[11] Auber JC, Bibaut A, Rigal MJ. Characterization of multipath on land and sea at GPS frequencies. In: ION GPS-94; Sept. 1994; Salt Lake City, UT. p. 1155-1171

[12] Garrison JL, Katzberg SJ, Hill MI. Effect of sea roughness on bistatically scattered range coded signals from the global positioning system. Geophysical Research Letters. 1998; **25**(13):2257-2260. DOI: 10.1029/98GL51615

[13] Lowe S, LaBrecque JL, Zuffada C, Romans LJ, Young LE, Hajj GA. First spaceborne observation of an earth-reflected GPS signal. Radio Science. 2002;**37**(1):1-28. DOI: 10.1029/2000RS002539

[14] Gleason ST, Hodgart S, Yiping S, Gommenginger C, Mackin S, Adjrad M, Unwin M. Detection and processing of bistatically reflected GPS signals from low earth orbit for the purpose of ocean remote sensing. IEEE Transactions on Geoscience and Remote Sensing. 2005;**43**(6):1229-1241. DOI: 10.1109/TGRS.2005.845643

[15] Unwin M, Duncan S, Jales P, Blunt P, Brenchley M. Implementing GNSS reflectometry in space on the TechDemoSat-1 mission. In: Proc. Institute Navigation; 2014; Tampa, Florida. p. 1222-1235

[16] Martin-Neira M, D'Addio S, Buck C, Floury N, Prieto-Cerdeira R. The PARIS ocean altimeter in-orbit demonstrator. IEEE Transactions on Geoscience and Remote Sensing. 2011;**49**(6):2209-2237. DOI: 10.1109/TGRS.2010.2092431

[17] Wickert J, Andersen O, Beyerle G, Cardellach E, Chapron B, Gommenginger C, Hatton J, Høeg P, Jäggi A, Jakowski N, Kern M, Lee T, Martin-Neira M, Montenbruck O, Pierdicca N, Rius A, Shum CK, Zuffada C. Innovative remote sensing using the International Space Station: GNSS reflectometry with GEROS. In: Proc. IEEE Int. Geoscience Remote Sensing Symp; 2014; Québec, Canada

[18] Ruf CS, Gleason S, Jelenak Z, Katzberg S, Ridley A, Rose R, Scherrer J, Zavorotny V. The CYGNSS nanosatellite constellation hurricane mission. In: Proc. IEEE Int. Geoscience Remote Sensing Symp; 2012; Munich, Germany. pp. 214–216

[19] Zavorotny VU, Voronovich AG. Scattering of GPS signals from the ocean with wind remote sensing application. IEEE Transactions on Geoscience and Remote Sensing. 2000; **38**(1):951-964. DOI: 10.1109/36.841977

[20] Marchan JF, Alvarez NR, Valencia E, Ramos-Perez I. An efficient algorithm to the simulation of delay–Doppler maps of reflected global navigation satellite system signals. IEEE Transactions on Geoscience and Remote Sensing. 2009;**47**(8):2733-2740. DOI: 10.1109/TGRS.2009.2014465

[21] Garrison JL. A statistical model and simulator for ocean-reflected GNSS signals. IEEE Transaction on Geoscience and Renote Sensing. 2016;**54**(10):6007-6019. DOI: 10.1109/TGRS.2016.2579504

[22] Clarizia MP, Gommeninger C, Di Bisceglie M, Galdi C, Srokosz MA. Simulation of L-band bistatic returns from the ocean surface: A facet approach with application to ocean GNSS reflectometry. IEEE Transactions on Geoscience and Remote Sensing. 2012;**50**(3): 960-971. DOI: 10.1109/TGRS.2011.2162245

[23] Lowe ST, Kroger P, Franklin G, LaBrecque JL, Lerma J, Lough Ml, Marcin MR, Muellerschoen RJ, Spitzmesser D, Young LE. A delay/Doppler-mapping receiver system for GPS-reflection remote sensing. IEEE Transactions on Geoscience and Remote Sensing. 2002;**40**(5):1150-1163. DOI: 10.1109/TGRS.2002.1010901

[24] Nogués-Correig O, Galí El C, Campderrós JS, Rius A. A GPS-reflections receiver that computes Doppler/delay maps in real time. IEEE Transactions on Geoscience and Remote Sensing. 2007;**45**(1):156-174. DOI: 10.1109/TGRS.2006.882257

[25] Steenwijk R, Unwin M, Jales P. A next generation spaceborne GNSS receiver for navigarion and remote sensing. In: Satellite Navigation Technoloies and Ruropean Workshop on GNSS Signals and Signal Processing; 2010; Noordwijk, Netherlands

[26] Wickert J, Cardellach E, Martin-Neria M, et al. GEROS-ISS: GNSS REflectometry, radio Occulation and Scatterometry Onboard the international Space Station. IEEE Journal of Selected Topics in Applied Earth Observations and Remote Sensing. 2016;**9**(10):4552-4581. DOI: 10.1109/JSTARS.2016.2614428

[27] Garrison JL, Komjathy A, Zavorotny VU, Katzberg SJ. Wind speed measurements using forward scattered GPS signals. IEEE Transactions on Geoscience and Remote Sensing. 2002;**40**(1):50-65. DOI: 10.1109/36.981349

[28] Li C, Huang W. An algorithm for sea-surface wind field retrieval from GNSS-R delay_ doppler map. IEEE Geoscience and Remote Sensing Letters. 2014;**11**(12):2110-2114. DOI: 10.1109/LGRS.2014.2320852

[29] Rodriguez-Alvarez N, Akos DM, Zavorotny VU, Smith JA, Camps A, Fairall CW. Airborne GNSS-R wind retrievals using delay-Doppler maps. IEEE Transactions on Geoscience and Remote Sensing. 2013;**51**(1):626-641. DOI: 10.1109/TGRS.2012.21-96437

[30] Foti G, Gommenginger C, Jales P, Unwin M, Shaw A, Robertson C, Roselló J. Spaceborne GNSS reflectometry for ocean winds: First results from the UK TechDemoSat-1 mission. Geophysical Research Letters. 2015;**42**:5435-5441. DOI: 10.1002/2015GL064204

[31] Rodriguez-Alvarez N, Garrison JL. Generalized linear observables for ocean wind retrieval from calibrated GNSS-R delay-Doppler maps. IEEE Transactions on Geoscience and Remote Sensing. 2016;**52**(2):1142-1155. DOI: 10.1109/TGRS.2015. 2475317

[32] Clarizia MP, Ruf CS. Wind speed retrieval algorithm for the Cyclone Global Navigation Satellite System (CYGNSS) misson. IEEE Transactions on Geoscience and Remote Sensing. 2016;**54**(8):4419-4432. DOI: 10.1109/TGRS.2016.2541343

[33] Valencia E, Camps A, Marchan-Hernandez JF, Park H, Bosch-Lluis X, Rodriguez-Alvarez N, Ramos-Perez I. Ocean surface's scattering coeggicient retrieval by delay-Doppler map inversion. IEEE Geoscience and Remote Sensing Letters. 2011;**8**(4):750-754. DOI: 10.1109/LGRS.2011.2107500

[34] Schiavulli D, Nunziata F, Migliaccio M, Frappart F, Ramilien G, Darrozes J. Reconstruction of the radar image from actual DDMs collected by TechDemoSat-1 GNSS-R mission. IEEE Journal of Selected Topics in Applied Earth Observations and Remote Sensing. 2016; **9**(10):4700-4708. DOI: 10.1109/JSTARS.2016.2543301

[35] Marchan JF, Camps A, Rodriguez Alvarez N, Bosch X, Ramos-Perez I, Valencia E. PAU/GNSS-R: Implementation, performance and first results of a real-time delay-Doppler map reflectometer using global navigation satellite system signals. Sensors. 2008;**8**:3005-3019. DOI: 10.3390/s8053005

[36] Carrneo-Luengo H, Camps A, Ramos-P'erez I, Rius A. Experimental evaluation of GNSS-reflectometyr altimetric precision using P(Y) and C/A signals. IEEE Journal of Selected Topics in Applied Earth Observations and Remote Sensing. 2014;**7**(5):1493-1500. DOI: 10.1109/JSTARS.2014.2320298

[37] Carreno-Luengo H, Camps A, Perez-Ramos I, Rius A. Pycaro's instrument proof of concept. In: Proc. Workshop ReflectometryUsing GNSS Other Signals Opportunity (GNSS+R); West Lafayette, IN; 2012. pp. 1–4

[38] Han L, Meng Y, Wang Y, Han X. A fast algorithm of GNSS-R signal processing based on DBZP. In: China Satellite Navigation Conference (CSNC); 2017; Shanghai, China. pp. 187-197

[39] Gleason S. Space-based GNSS Scatterometry: Ocean wind sensing using an empirically calibrated model. IEEE Transactions on Geoscience and Remote Sensing. 2013;**51**(9):4853-4863. DOI: 10.1109/TGRS.2012.2230401

[40] Clarizia MP, Ruf CS. On the spatial resolution of GNSS reflectometry. IEEE Geoscience and Remote Sensing Letters. 2016;**13**(9):1064-1068. DOI: 10.1109/LGRS. 2016.2565380

[41] Soisuvarn S, Jelenak Z, Said F, et al. The GNSS reflectometry response to the ocean surface winds and waves. IEEE Journal of Selected Topics in Applied Earth Observations & Remote Sensing. 2016;**9**(10):4678-4699. DOI: 10.1109/JSTARS. 2016.2602703